Global contrail coverage simulated by CAM5 with the inventory of 2006 global aircraft emissions

Chih-Chieh Chen,[1] Andrew Gettelman,[1,2] Cheryl Craig,[1] Patrick Minnis,[3] and David P. Duda[4]

Received 1 November 2011; revised 1 November 2011; accepted 8 February 2012; published 4 April 2012.

[1] This paper documents the incorporation of an inventory of the AEDT (Aviation Environmental Design Tool) global commercial aircraft emissions for the year of 2006 into the National Center for Atmospheric Research Community Earth System Model (CESM) version 1. The original dataset reports aircraft emission mass of ten species on an hourly basis which is converted to monthly emission mixing ratio tendencies as the released version of the dataset. We also describe how the released aircraft emission dataset is incorporated into CESM. A contrail parameterization is implemented in the CESM in which it is assumed that persistent contrails initially form when aircraft water vapor emissions experience a favorable atmospheric environment. Both aircraft emissions and ambient humidity are attributed to the formation of contrails. The ice water content of contrails is assumed to follow an empirical function of atmospheric temperature which determines the cloud fraction associated with contrails. Our modeling study indicates that the simulated global contrail coverage is sensitive to the vertical resolution of the GCMs in the upper troposphere and lower stratosphere because of model assumptions about the vertical overlap structure of clouds. Furthermore, the extent of global contrail coverage simulated by CESM exhibits a seasonal cycle which is in broad agreement with observations.

Citation: Chen, C.-C., A. Gettelman, C. Craig, P. Minnis, and D. P. Duda (2012), Global contrail coverage simulated by CAM5 with the inventory of 2006 global aircraft emissions, *J. Adv. Model. Earth Syst.*, *4*, M04003, doi:10.1029/2011MS000105.

1. Introduction

[2] Aircraft emissions may have significant impacts on atmospheric chemistry and climate [*Henderson et al.*, 1999; *Lee et al.*, 2010]. Aircraft emit carbon dioxide (CO_2), and contribute about 3% to total atmospheric CO_2 emissions [*Penner et al.*, 1999]. Aircraft also emit nitrogen oxides (NO_X) that may increase ozone in the upper troposphere and lower stratosphere as well as increase the destruction of methane. It is now understood that the climate impact of these effects offset each other. Particulates (soot) and gas emissions (SO_2) from aircraft may also alter natural cirrus cloud properties by acting as additional ice nuclei [*Kärcher et al.*, 2007]. Aircraft emissions are continuing to and expected to increase dramatically in the coming decades [*Lee et al.*, 2010], so the impacts on the atmosphere will increase.

[3] Aircraft also form contrails from their exhaust of water vapor as it rapidly cools and mixes, forming liquid drops that freeze. These ice clouds form when the atmosphere is cold enough and the humidity is high enough [*Appleman*, 1953]. If in addition the air is supersaturated, these contrails may persist, and take up water vapor from ambient air. These persistent contrails may last minutes up to several hours [*Minnis et al.*, 1998]. Like cirrus, contrails have a radiative forcing effect on climate [*Marquart and Mayer*, 2002], cooling in the shortwave by reflecting radiation to space, but heating in the longwave, because they have a low emission temperature. The longwave effect is thought to dominate for these clouds, because of their low temperatures [*Stephens and Webster*, 1981; *Hartmann et al.*, 1992; *Meerkötter et al.*, 1999]. The effect of this radiative forcing is highly local in time and space with the distribution of aircraft traffic in the upper troposphere. The local and global effects are highly uncertain [*Henderson et al.*, 1999; *Lee et al.*, 2010]. Globally they are on the order of 0.01 to 0.5 Wm^{-2}, as large as the contribution to anthropogenic radiative forcing from CO_2 emitted by aircraft.

[4] Several recent studies have addressed anthropogenic climate change induced by aircraft emission [*Penner et al.*, 1999; *Minnis et al.*, 1999; *Myhre and Stordal*, 2001; *Marquart and Mayer*, 2002; *Meyer et al.*, 2002; *Rädel and Shine*, 2008; *Burkhardt et al.*, 2010].

[1]National Center for Atmospheric Research, Boulder, Colorado, USA.
[2]Institute for Atmospheric and Climate Science, ETH Zurich, Zurich, Switzerland.
[3]NASA Langley Research Center, Hampton, Virginia, USA.
[4]Science Systems and Applications, Inc., Hampton, Virginia, USA.

1942-2466/12/2011MS000105

Simulating the potential climate and chemical impacts of all these aviation emissions requires several important pieces. In this study, we document the development of new modules for an advanced General Circulation Model (GCM) that incorporates aircraft emissions to simulate these effects. The model is the National Center for Atmospheric Research (NCAR) Community Earth System Model (CESM) and its atmospheric component, the Community Atmosphere Model (CAM).

[5] This paper briefly describes the base model and a comprehensive emission inventory of commercial aircraft emissions (Section 2). We then describe how the emission inventory of gases and particles from aircraft is converted to inputs for the GCM (section 3). Section 4 describes how these species interact with the model state, focusing on integration with model cloud microphysics and aerosols to generate contrails. Preliminary results are presented with discussion in Section 5 and links to the code in Appendix A.

2. Tools

2.1. Model Description

[6] This work uses CAM version 5. CAM5 is described by [*Gettelman et al.*, 2010; *Neale et al.*, 2010] (P. J. Rasch et al., Scientific description and performance of the Community Atmosphere Model version 5, manuscript in preparation, 2012) and its salient features are briefly described here. The model includes a detailed treatment of cloud liquid and ice microphysics, including a representation of particle size distributions, a detailed mixed phase and ice supersaturation. This is coupled to a consistent radiative treatment of ice clouds, and an aerosol model that includes particle effects on liquid and ice clouds. CAM5 uses a 4 class (liquid, ice, rain and snow), 2-moment stratiform cloud microphysics scheme described by *Morrison and Gettelman* [2008] and implemented as described by *Gettelman et al.* [2008, 2010]. The model radiation code has been updated to the Rapid Radiative Transfer Model for GCMs (RRTMG) described by *Iacono et al. [2008]*, and a new radiation interface developed for the microphysics. The liquid cloud macrophysical closure is described by S. Park and C. S. Bretherton (Revised stratiform macrophysics in the Community Atmosphere Model, manuscript in preparation, 2012).

[7] The aerosol treatment in the model uses a modal based scheme similar to that described by *Easter et al.* [2004], but with only three modes (Aitken, accumulation, and coarse). The predicted internally-mixed aerosol species include sulfate, sea salt, secondary organic aerosols, soil dust, black carbon and primary organic carbon. Ammonium is diagnosed from sulfate assuming sulfate is partially neutralized by the form of $NH_4H_2SO_4$. *Liu et al.* [2011] shows that this scheme yields results very similar to a more complete seven-mode scheme that predicts ammonia and includes separate modes for primary carbonaceous aerosol and coarse and fine sea salt and soil dust.

[8] CAM5 can be run under prescribed meteorology or so-called specified dynamics (CAM5-SD). Under this mode, the winds, temperature, and water vapor (optional) fields are nudged to a prescribed climatology. In this study, we use a climatology produced by CAM5 under the free running mode and the model state variables are output every 6 hours to drive the CAM5-SD runs. In our CAM5-SD runs, the water vapor field is read in from prescribed climatology.

[9] One new attribute of CAM5 is that it allows ice supersaturation. For model validation purposes, here we present the frequency of ice supersaturation and relative humidity from the Atmospheric Infra Red Sounder (AIRS) satellite [*Gettelman et al.*, 2006] and those simulated by CAM5-SD. As illustrated in Figure 1, CAM5-SD does a reasonable job in simulating the mean relative humidity in the upper troposphere and lower stratosphere (UTLS) as revealed in Figure 1c and 1d. Relative humidity in CAM5-SD is about 50% higher than AIRS throughout much of the UTLS. This is not surprising, since AIRS is a nadir IR sounder that cannot see in regions of clouds, and has a dry bias relative to UTLS observations [*Gettelman et al.*, 2006]. The distribution of relative humidity is similar to observations, peaking in the upper troposphere below the tropopause, in high-latitudes and in the tropical tropopause layer (TTL). The frequency of ice supersaturation in CAM5-SD (Figure 1b) is also higher than AIRS, but has a similar distribution, peaking at about 400 hPa in high latitudes, at slightly lower pressures in the sub-tropics, and at higher frequencies in the tropical UTLS. The hemispheric asymmetry in ice supersaturation frequency (higher in the S. Hemisphere) is also reproduced (Figure 1a and 1b).

2.2. Dataset

[10] Recently, we obtained the Aviation Environment Design Tool (AEDT) dataset which is a global inventory of aircraft emissions [*Wilkerson et al.*, 2010; *Kim et al.*, 2007; *Lee et al.*, 2007]. The AEDT dataset reports aircraft emissions for the entire year of 2006. The dataset is in the ASCII format and only reports grid cells with non-zero emission mass. Hence, the dataset is very sparse and does not serve well as an input file for numerical model simulations.

[11] The AEDT dataset is an hourly inventory of global aircraft emission mass of ten emission species over a $1^\circ \times 1^\circ$ latitude-longitude mesh with a vertical spacing of 150 m in the year of 2006 (see Table 1 for a list of emission species). The original dataset only reports grid cells with non-zero emission mass.

3. Data Conversion

[12] To integrate the emissions data set with the model, we convert it to emissions mass mixing ratio rates on the model grid. Such conversion requires information about the mass of air in each grid cell which may be calculated given the vertical distribution of pressure and temperature.

[13] To achieve this task, we use monthly climatology files derived from a long-term simulation by the Community Atmosphere Model (CAM) of $1.9^\circ \times 2.5^\circ$ latitude-longitude resolution with 30 vertical layers.

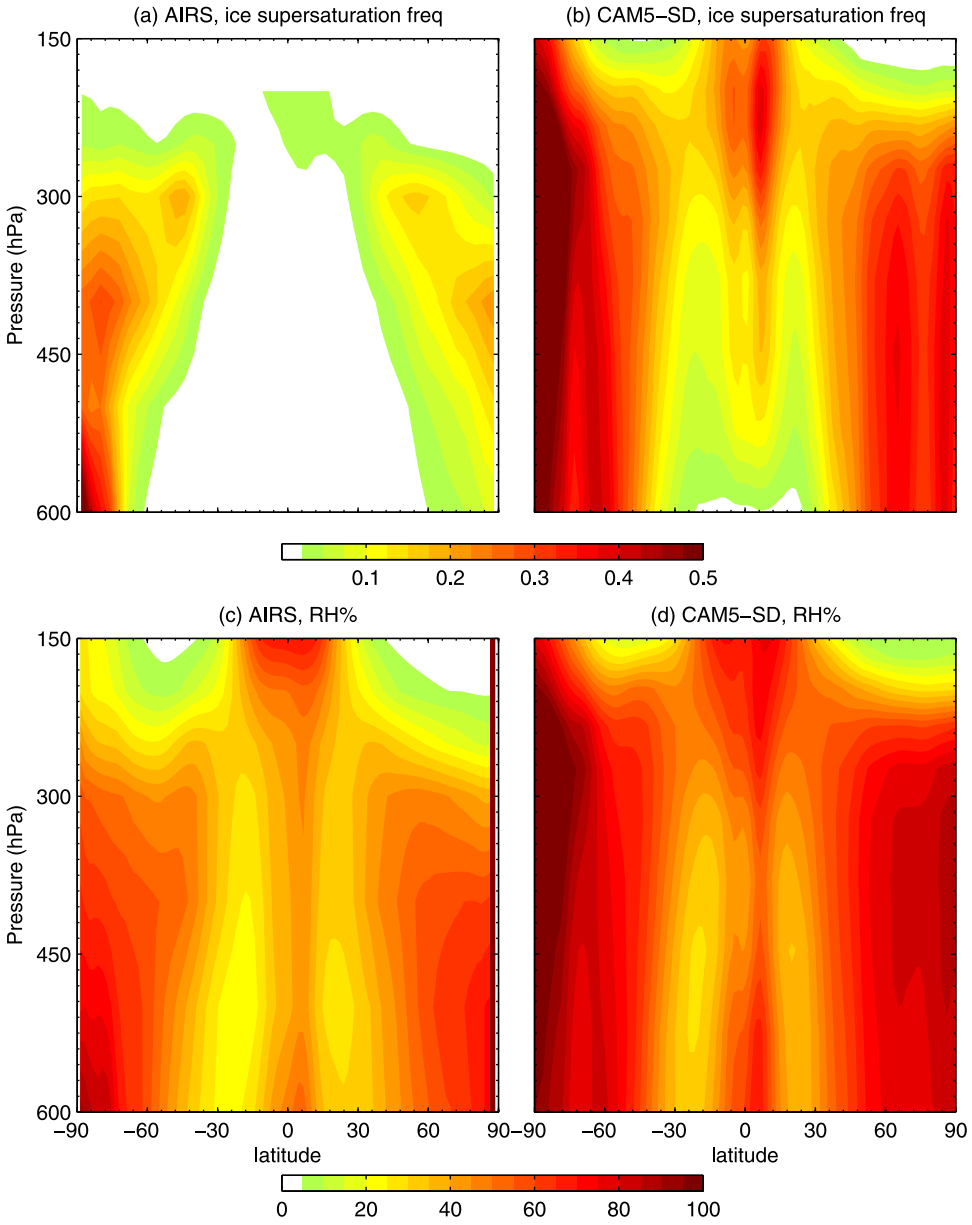

Figure 1. Zonally mean annual frequency of ice supersaturation and relative humidity simulated by (a, c) AIRS and (b, d) CAM5 observations [*Gettelman et al.*, 2006].

Pressure at model interfaces in CAM is anchored by surface pressure (p_s), i.e.,

$$p_{i,j,k+\frac{1}{2}} = a_{k+\frac{1}{2}} \cdot p_{s_{i,j}} + b_{k+\frac{1}{2}} \cdot p_0, \tag{1}$$

where $p_0 = 10^3$ hPa is a reference pressure. The geopotential height at model interfaces may be calculated by

$$\tilde{z}_{i,j,k-\frac{1}{2}} = \tilde{z}_{i,j,k+\frac{1}{2}} + \frac{R_d \tilde{T}_{v_{i,j,k}}}{g} \left(\ln \tilde{p}_{i,j,k+\frac{1}{2}} - \ln \tilde{p}_{i,j,k-\frac{1}{2}} \right), \tag{2}$$

where R_d is the gas constant for dry air, $\tilde{T}_v$ the virtual temperature, g the gravitational acceleration, and p the pressure. Note that $\tilde{z}_{30+\frac{1}{2}} = \tilde{z}_s$ is surface elevation and $\tilde{p}_{30+\frac{1}{2}} = \tilde{p}_s$ is surface pressure. Pressure and geopotential height are then interpolated to the horizontal grid of $1^\circ \times 1^\circ$ latitude-longitude resolution, i.e., $(\tilde{z}_k, \tilde{p}_k) \rightarrow (z_k, p_k)$.

[14] The emission mass is first summed monthly which is denoted as $M_{i,j,k}$. The monthly emission mass is binned into the CAM vertical resolution based on geopotential height at model interfaces (z_k), denoted as $m_{i,j,k}$. The monthly emission mass may be converted to monthly emission mixing ratio by division of air mass in each grid cell. The area for the grid cell centered at (latitude, longitude) = (ϕ_j, λ_i), is

$$A_{i,j} = \int_{\lambda_{i-\frac{1}{2}}}^{\lambda_{i+\frac{1}{2}}} \int_{\phi_{j-\frac{1}{2}}}^{\phi_{j+\frac{1}{2}}} R_E^2 \cos\phi \, d\phi \, d\lambda$$

$$= R_E^2 \left(\sin \phi_{j+\frac{1}{2}} - \sin \phi_{j-\frac{1}{2}} \right) \left(\lambda_{i+\frac{1}{2}} - \lambda_{i-\frac{1}{2}} \right), \tag{3}$$

Table 1. Information Included in the AEDT 2006 Aircraft Emission Dataset

Field	Units	Description
MONTH	N/A	Month of the year
DAY	N/A	Day of the month
HOUR	N/A	Hour in GMT (00 to 23)
LAT INDEX	N/A	Latitude Index (I)
LON INDEX	N/A	Longitude Index (J)
SLANT DIST	Nautical Miles	Aggregated Flight Path Distance in Grid Cell
TRACK DIST	Nautical Miles	Aggregated Ground Projected Path Distance in Grid Cell
FUELBURN	Kilograms	Total Fuelburn in Grid Cell
CO	Grams	Total Mass of CO emissions in Grid Cell
HC	Grams	Total Mass of HC emissions in Grid Cell
NOX	Grams	Total Mass of NO_X emissions in Grid Cell
PMNV	Grams	Total Mass of Non Volatile particulate mass emissions in Grid Cell
PMSO	Grams	Total Mass of Sulfur organics particulate emissions in Grid Cell
PMFO	Grams	Total Mass of Fuel organics particulate emissions in Grid Cell
CO2	Grams	Total Mass of CO_2 emissions in Grid Cell
H2O	Grams	Total Mass of H_2O emissions in Grid Cell
SOX	Grams	Total Mass of SO_X emissions in Grid Cell

where R_E is the radius of Earth. The emission mass ($m_{i,j,k}$) may be further converted to emission mixing ratio ($q_{i,j,k}$) by division of air mass for each grid cell, i.e.,

$$q_{i,j,k} = \frac{m_{i,j,k}}{A_{i,j}\left(p_{i,j,k+\frac{1}{2}} - p_{i,j,k-\frac{1}{2}}\right)/g}. \quad (4)$$

Finally, emission mixing ratio tendency (q_t) is obtained by division of time in seconds for each month and it is stored in the released netCDF files.

[15] The converted data in Jan. and Jul. are illustrated for fuel burned (Figure 2). In addition to fuel burned, emission rates (in kg/kg/s) have been calculated for all other emission species in Table 1. Note that the AEDT emissions use constant emission factors as a function of fuel burned for CO_2, H_2O, PMFO, PMSO, and SO_X so these species emissions are linearly related to fuel burned.

[16] Figure 2 indicates that the largest emissions take place in mid latitudes of the Northern Hemisphere around 200 hPa (Figure 2a and 2b). This is the region where most flight tracks are found. Based on the emission distribution at 198 hPa (Figure 2c and 2d), even individual flight routes may be identified. Aircraft cruise at roughly the same pressure levels during the year, resulting similar emission tendencies at 198 hPa between Jan. and Jul. This has important implications for the formation of contrails which requires a moist and cold ambient environment. Higher tropopause altitudes in summer significantly increase the portion of emissions in the troposphere to potentially form contrails while emissions in the stratosphere do not [*Gettelman and Baughcum*, 1999; *Burkhardt et al.*, 2008]. Nevertheless, warmer atmospheric temperature in the upper troposphere in summer may serve to reduce the formation of contrails.

[17] The flight path distance of the ADET dataset, SLANT DIST and TRACK DIST in Table 1, is treated slightly differently. The flight path distance is simply binned in the vertical and converted to rate of distance traveled in each grid cell during the data conversion process. The converted data are illustrated in Figure 3 which shows similar features as found in Figure 2 with one major difference of larger values for the flight path distance (Figures 3a and 3b) in the mid troposphere since it is not converted to a mixing ratio. Flight distance traveled in a grid cell is used in initializing contrails as described below.

[18] The Community Earth System Model version 1.0.2 (CESM1.0.2) and later includes the functionality of incorporating aircraft emission mixing ratio tendencies into the model simulation. Details about this functionality are documented in Appendix A.

[19] When emissions are incorporated in CESM simulations, horizontal and vertical interpolation of the emission mixing ratio tendencies is usually necessary because the horizontal resolution of the model run and the surface pressure field may be different from those in the dataset. In the release, we have an updated interpolation algorithm to ensure the global emission mass is conserved during the interpolation process. The new algorithm assumes a uniform emission mixing ratio tendency within each grid cell and the interpolation aims at preserving the quantity of

$$\int_{p_t}^{p_s}\int_{-\frac{\pi}{2}}^{\frac{\pi}{2}}\int_{0}^{2\pi} q_{t_{i,j,k}} \cos\phi \, d\lambda \, d\phi \, dp, \quad (5)$$

or in the discrete form of

$$\sum_{k=1}^{k_m}\sum_{j=1}^{j_m}\sum_{i=1}^{i_m} q_{t_{i,j,k}}\left(\sin\phi_{j+\frac{1}{2}} - \sin\phi_{j-\frac{1}{2}}\right)\left(\lambda_{i+\frac{1}{2}} - \lambda_{i-\frac{1}{2}}\right)\left(p_{i,j,k+\frac{1}{2}} - p_{i,j,k-\frac{1}{2}}\right), \quad (6)$$

assuming there are i_m longitudinal points, j_m latitudinal points, and k_m vertical layers.

[20] The newly implemented interpolation scheme has longitudinal, latitudinal, and vertical components and only acts on the aircraft emissions but not on other aerosol species. The mixing ratio tendency is assumed to be a step function in each grid cell. For an interpolation

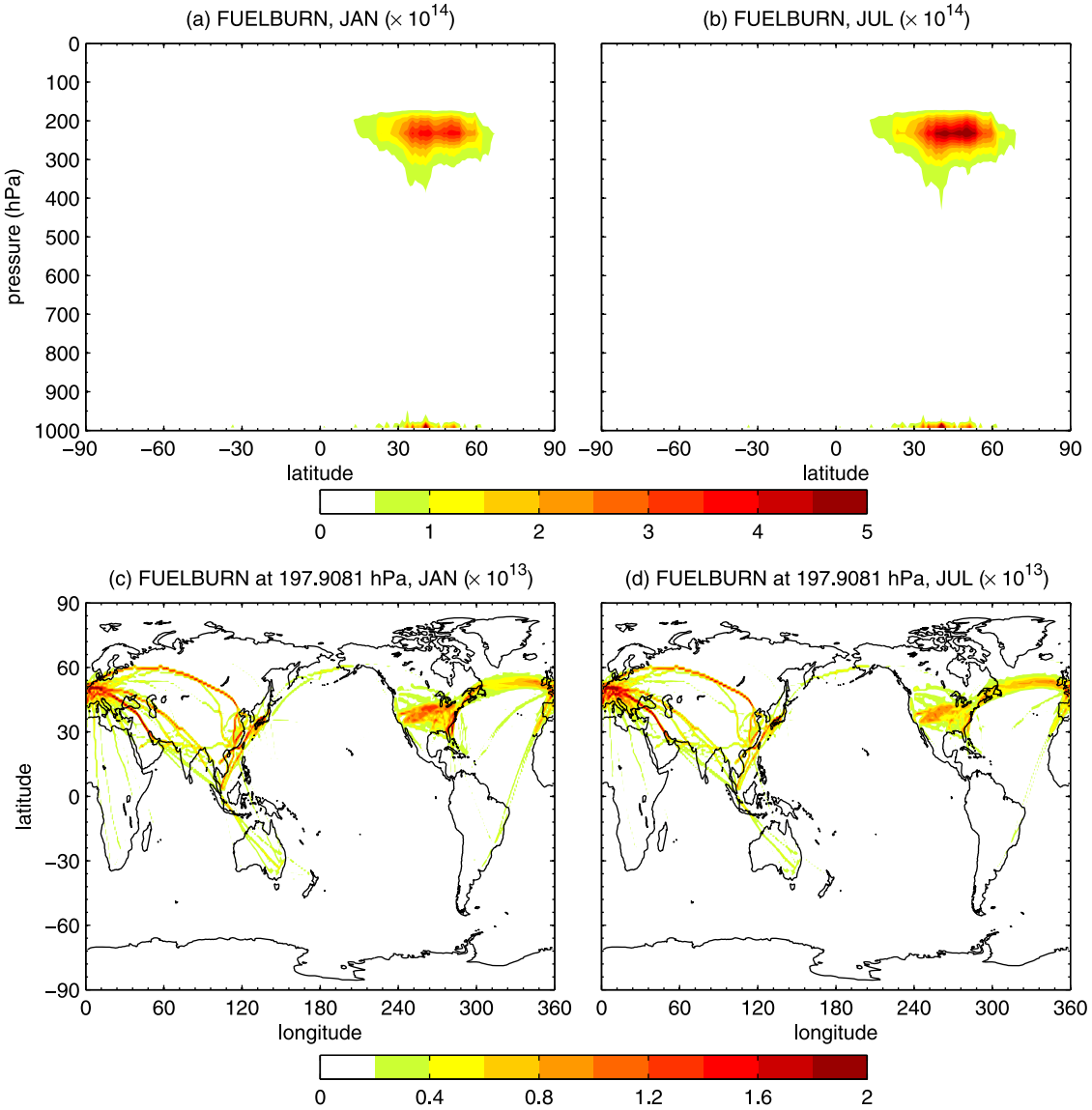

Figure 2. Aircraft fuelburn mixing ratio tendency in kg/kg/s: (a) zonal average in Jan., (b) zonal average in Jul., (c) at $p = 197.9081$ hPa in Jan., and (d) at $p = 197.9081$ hPa in Jul.

from $(q_t, \lambda, \phi, p, i_m, j_m, k_m)$ to $\left(\hat{q}_t, \hat{\lambda}, \hat{\phi}, \hat{p}, I_M, J_M, K_M\right)$, the three components achieve, respectively,

$$\sum_{i=1}^{i_m} q_{t_{i,j,k}} \left(\lambda_{i+\frac{1}{2}} - \lambda_{i-\frac{1}{2}}\right) = \sum_{i=1}^{I_M} \hat{q}_{t_{i,j,k}} \left(\hat{\lambda}_{i+\frac{1}{2}} - \hat{\lambda}_{i-\frac{1}{2}}\right), \quad (7)$$

$$\sum_{j=1}^{j_m} q_{t_{i,j,k}} \left(\sin\phi_{j+\frac{1}{2}} - \sin\phi_{j-\frac{1}{2}}\right) = \sum_{j=1}^{J_M} \hat{q}_{t_{i,j,k}} \left(\sin\hat{\phi}_{j+\frac{1}{2}} - \sin\hat{\phi}_{j-\frac{1}{2}}\right), \quad (8)$$

$$\sum_{k=1}^{k_m} q_{t_{i,j,k}} \left(p_{i,j,k+\frac{1}{2}} - p_{i,j,k-\frac{1}{2}}\right) = \sum_{k=1}^{K_M} \hat{q}_{t_{i,j,k}} \left(\hat{p}_{i,j,k+\frac{1}{2}} - \hat{p}_{i,j,k-\frac{1}{2}}\right). \quad (9)$$

Hence, the interpolation algorithm conserves global emission mass, i.e.,

$$\sum_{k=1}^{k_m} \sum_{j=1}^{j_m} \sum_{i=1}^{i_m} q_{t_{i,j,k}} \left(\sin\phi_{j+\frac{1}{2}} - \sin\phi_{j-\frac{1}{2}}\right) \left(\lambda_{i+\frac{1}{2}} - \lambda_{i-\frac{1}{2}}\right) \left(p_{i,j,k+\frac{1}{2}} - p_{i,j,k-\frac{1}{2}}\right) = \sum_{k=1}^{K_M} \sum_{j=1}^{J_M} \sum_{i=1}^{I_M} \hat{q}_{t_{i,j,k}} \left(\sin\hat{\phi}_{j+\frac{1}{2}} - \sin\hat{\phi}_{j-\frac{1}{2}}\right) \left(\hat{\lambda}_{i+\frac{1}{2}} - \hat{\lambda}_{i-\frac{1}{2}}\right) \left(\hat{p}_{i,j,k+\frac{1}{2}} - \hat{p}_{i,j,k-\frac{1}{2}}\right). \quad (10)$$

4. Incorporation Into Model Physics

[21] The emissions in the model are added as tendencies for chemical species, aerosols and water. Water substance is added as either vapor or ice, as described below.

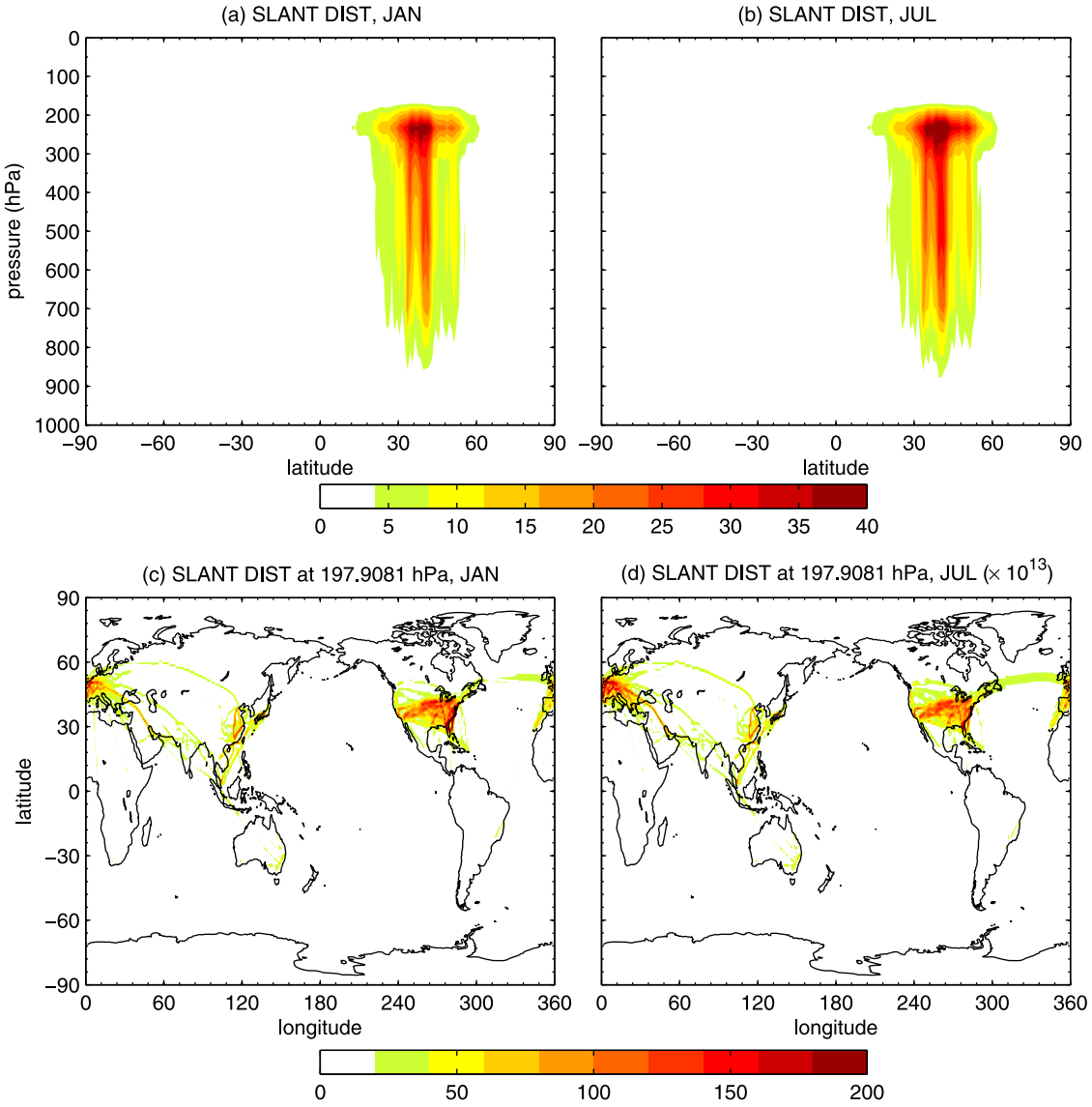

Figure 3. Aggregated fight path distance (SLANT DIST in Table 1) tendency in m/s: (a) zonal average in Jan., (b) zonal average in Jul., (c) at p = 197.9081 hPa in Jan., and (d) at p = 197.9081 hPa in Jul.

4.1. Chemical Species and Aerosols

[22] The time tendency of aerosol emissions (black carbon and sulfate) is simply added to their existing mass in the modal aerosol scheme. The particulate number concentrations are increased in proportion to their mass, simply assuming the size of emission of particles is the same as those already present in the model. Future studies can easily modify this assumption to make a different size assumption about aircraft particulate emissions.

4.2. Water Vapor Emissions

4.2.1. Contrail Parameterization

[23] Water vapor emissions from aircraft are input into the model either as water vapor or cloud ice determined by a contrail parameterization following the Schmidt-Appleman Criteria [*Schmidt*, 1941; *Appleman*, 1953] as described by *Schumann* [1996] and used by *Ponater et al.* [2002]. If the atmospheric conditions favor formation of persistent contrails, i.e., the ambient temperature is below a critical temperature and the ambient air is above ice saturation, water vapor emissions turn into ice along with some of the ambient humidity above ice supersaturation as noted below. Otherwise, water vapor emissions remain in the gas phase and they add to the water vapor field of the model.

[24] An empirical formula giving the critical temperature (T_c) for contrail formation where T_c is expressed in Celsius, as described by *Schumann* [1996], is

$$T_c = -46.46 + 9.43\ln(G - 0.053) + 0.72\left[\ln(G - 0.053)^2\right], \quad (11)$$

and G, with units of PaK^{-1}, is defined as

$$G = \frac{EI_{H_2O} \cdot c_p p}{\varepsilon Q(1-\eta)} \quad (12)$$

where c_p is the specific heat of air at constant pressure ($J kg_{air}^{-1} K^{-1}$), p is the atmospheric pressure (Pa), ϵ is the ratio of the molecular masses of water and air $((kg_{H_2O} mol^{-1})/(kg_{air} mol^{-1}))$, EI_{H_2O} is the emission index of water vapor (kg_{H_2O}/kg_{fuel}),η is the propulsion efficiency of the jet engine, and Q is the specific combustion heat ($J kg_{fuel}^{-1}$). In this study, we set $EI_{H_2O} = 1.21 \times 10^8$, $\eta = 0.3$, and $Q = 43 \times 10^6$ J kg^{-1} [*Schumann*, 1996]. The critical relative humidity (RH_c) for contrail formation depends on G, T_c, and the ambient temperature T and may be expressed as [*Ponater et al.*, 2002]

$$RH_c(T) = \left[G \cdot (T - T_c) + e_{sat}^L(T_c)\right] / e_{sat}^L(T), \quad (13)$$

where e_{sat}^L is the saturation pressure of water vapor with respect to the liquid phase. Contrails may potentially form if the ambient temperature T is lower than the critical temperature T_c and the ambient relative humidity RH is higher than the critical relative humidity RH_c ($RH > RH_c$). An obvious additional condition has to be met for long-lived (persistent) contrails: the ambient air should be supersaturated with respect to ice.

[25] If the Schmidt-Appleman criteria are met, emissions are input as ice and both the number of in-cloud ice particles and the cloud fraction are increased. In addition to aircraft water vapor emissions, the ambient humidity above ice supersaturation within the volume swept by the aircraft (v) also feeds into the formation of contrails. The volume swept out (v) is a product of the flight path distance (d, SLANT DIST) and a cross-sectional area ($\mathcal{C}$). Hence, the mixing ratio of ice mass ($\mathcal{M}$) when contrail formation is triggered over each time step (Δt) is

$$\mathcal{M} = q_t \Delta t + \frac{d \cdot \mathcal{C}}{V} \left(\chi - \chi_{sat}^i\right), \quad (14)$$

where q_t is the aviation water vapor emission mixing ratio tendency at a given grid cell and V is the volume of the grid cell, χ is the ambient specific humidity, and χ_{sat}^i is the saturation specific humidity with respect to ice under the ambient temperature and pressure.

[26] The sensitivity to the area swept out (v) is to be tested by setting different values for the cross-sectional area, $\mathcal{C}$. In this study, two cases for C were tested: 100 m in width and depth (100 m $\times$ 100 m) and 300 m in width and depth (300 m $\times$ 300 m). A 300 m $\times$ 300 m cross-sectional area is meant to represent the water vapor in a contrail grown over the first time step of emission or about 15-30 minutes, and is consistent with *Naiman et al.* [2011].

[27] We assume that the shape of the ice particles is spherical and the effective radius with a radius r which should be determined by observation. Therefore, the number of in-cloud ice particles ($\mathcal{N}$) is, for a time step Δt, increased by

$$\Delta \mathcal{N} = \frac{\mathcal{M}}{\rho_i \frac{4}{3} \pi r^3}, \quad (15)$$

where q_t is the water vapor emission mixing ratio tendency at a given grid cell and ρ_i is the density of ice. By prescribing different particle sizes, sensitivity tests may be performed.

[28] The enhancement of cloud fraction due to formation of persistent contrails is determined by assuming an empirical value for the In-Cloud Ice Water Content (ICIWC). Based on a series of in-situ observations in contrails over many measurement campaigns, [*Schumann*, 2002] have estimated this value as a function of temperature:

$$\mathrm{ICIWC}(gm^{-3}) = \exp(6.97 + 0.103 T(C^o)) \times 10^{-3}, \quad (16)$$

and the cloud fraction ($\mathcal{A}$) is increased as

$$\Delta \mathcal{A} = \frac{\mathcal{M}}{\mathrm{ICIWC}/\rho_a}, \quad (17)$$

where ρ_a is the density of air.

4.2.2. Results From CAM5-SD Simulations

[29] Here we present results from four CAM5-SD simulations over a $1.9^\circ \times 2.5^\circ$ latitude-longitude mesh driven by meteorology from a free running CAM5 simulation. The only difference in these four runs is the vertical resolution in the UTLS (between 150 and 300 hPa). These four configurations are: 1) default CAM5 configuration (30 layers, L30, ~30 hPa or 1000 m in UTLS), 2) 40-layer CAM (L40, ~10 hPa or 300 m in UTLS), 3) 54-layer CAM (L54, ~5 hPa or 160 m in UTLS), and 4) 82-layer CAM (L82, ~2.5 hPa or 80 m in UTLS). The initial condition and meteorology driving these simulations are interpolated into higher resolution by the piecewise parabolic method [*Colella and Woodward*, 1984; *Carpenter et al.*, 1990] from files under the 30-layer configuration. The radius of ice particles is assumed to be 5 μm as observed in fresh contrails at around 30 min based on the work by *Schröder et al.* [2000]. The contrail parameterization operates in a diagnostic mode, i.e., aircraft emissions are assumed not to interact with state variables and the lifetime of contrails is assumed to be the same as the physical time step (30 min).

[30] As illustrated in Figure 4, the global ice water mass in contrails reaches its highest level in L30 and converges to a lower value as the vertical resolution is increased. Convergence in global ice mass in contrails occurs in L40, with a vertical resolution of 300 m in the UTLS. This feature is found to be independent of the assumption for the cross-sectional area ($\mathcal{C}$). With L30 resolution in the UTLS, when the Schmidt-Appleman criteria are met in a grid cell, contrail formation takes place in a relatively deep layer. The higher resolution models divide a deeper layer in a lower resolution model into several layers and the Schmidt-Appleman criteria may only be satisfied in a portion of these shallower layers. Fewer layers above ice supersaturation imply less

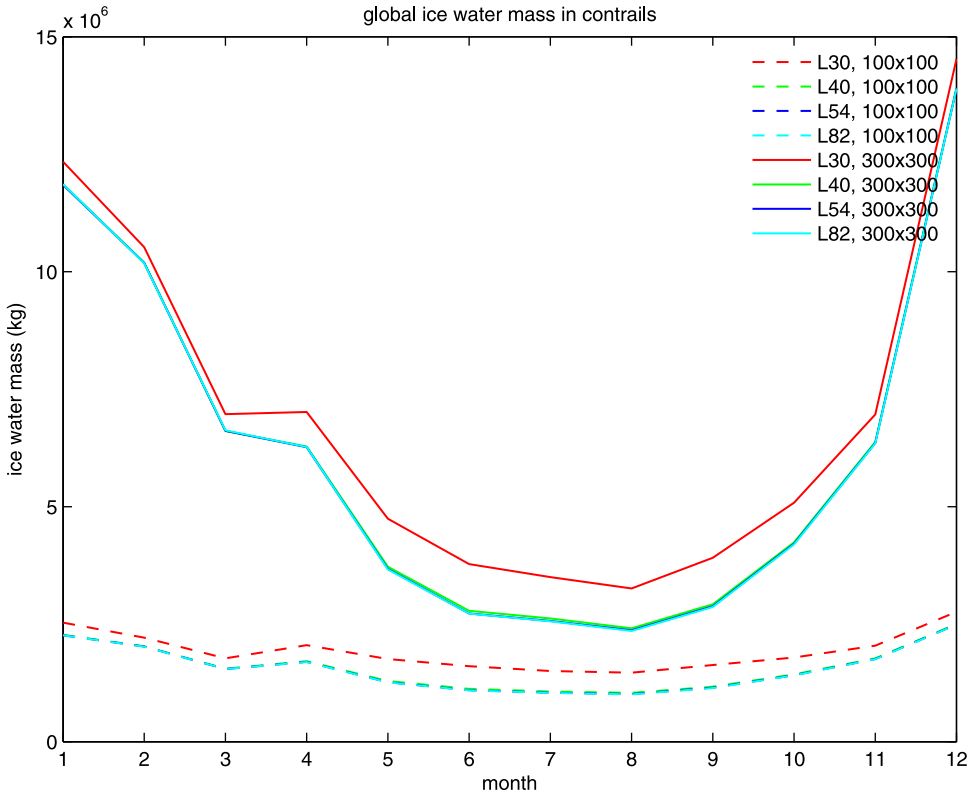

Figure 4. Average global ice water mass in contrails per time step (30 mins) simulated by four configurations (L30, L40, L54, and L82) of CAM5-SD by assuming a cross-sectional area of 100 m × 100 m and 300 m × 300 m.

uptake of humidity and less ice even if distance traveled and fuel burned are constant. Therefore, it leads to lower global ice water mass in higher resolution models.

[31] To evaluate the performance of CAM5 in producing reasonable contrail cloud fraction, retrievals from the Moderate Resolution Imaging Spectroradiometer (MODIS) radiance data are employed for comparison. The contrail fraction is determined from Aqua and Terra MODIS measurements using a version of the *Mannstein et al.* [1999] technique modified as described by *Minnis et al.* [2011] and *Duda et al.* [2011]. The Mannstein et al. method uses imagery from two thermal infrared channels (10.8 and 12.0 microns) of the Advanced Very High Resolution Radiometer (AVHRR) to detect linear contrails in both day and night scenes. It uses a scene-invariant threshold to detect cloud edges produced by contrails, and three binary masks to determine if the detected linear features are truly contrails. However, these masks are not always sufficient to remove all non-contrail features. *Palikonda et al.* [2005] estimated that linear contrail coverage was overestimated by approximately 40 percent over the contiguous United States (CONUS) from NOAA-15 and NOAA-16 AVHRR measurements. To reduce the number of false positive detections, observations from other thermal infrared radiance channels on MODIS are used to screen out linear cloud and surface features that appear as contrails in the original method. The contrail fraction determined from the modified contrail detection algorithm (CDA) was calibrated by using an updated version of the interactive program developed by *Minnis et al.* [2005] to perform a subjective visual error analysis on 44 MODIS images by 4 human analysts. The sensitivity of the CDA is adjusted so that the contrail fraction determined from the automated method matches the composite contrail fraction determined from the visual analysis. It is recognized that the selected CDA probably underestimates the actual contrail coverage because it missed many older, wider contrails that occur in clusters [*Duda et al.*, 2011]. Thus, the coverage may be more representative of younger linear contrail coverage than of linear contrails in general.

[32] The annually averaged cloud fraction distribution attributed to persistent contrails simulated by the CAM5-L82 model with an assumption of $\mathcal{C}$ = 300 m × 300 m is shown in Figure 5 which is the column sum of additional cloud fraction due to contrails. As expected, more cloud cover is found over the US and Western Europe where heavy air traffic takes place. Our contrail parameterization under CAM5-L82 is found to produce cloud fraction distributions and gradients similar to MODIS but with lower magnitude (by about a factor of 3) than the analysis from MODIS (compare Figure 5b with Figure 6). This is not unexpected since the lifetime of contrails in our CAM5 simulations is assumed to be 30 mins and their presence is instantaneous since they are all assumed to vanish at the end of each time step. Thus we expect our estimates should be lower than observations since we neglect longer lifetimes and spreading of contrails. These will be treated in a future analysis of the radiative forcing of contrails.

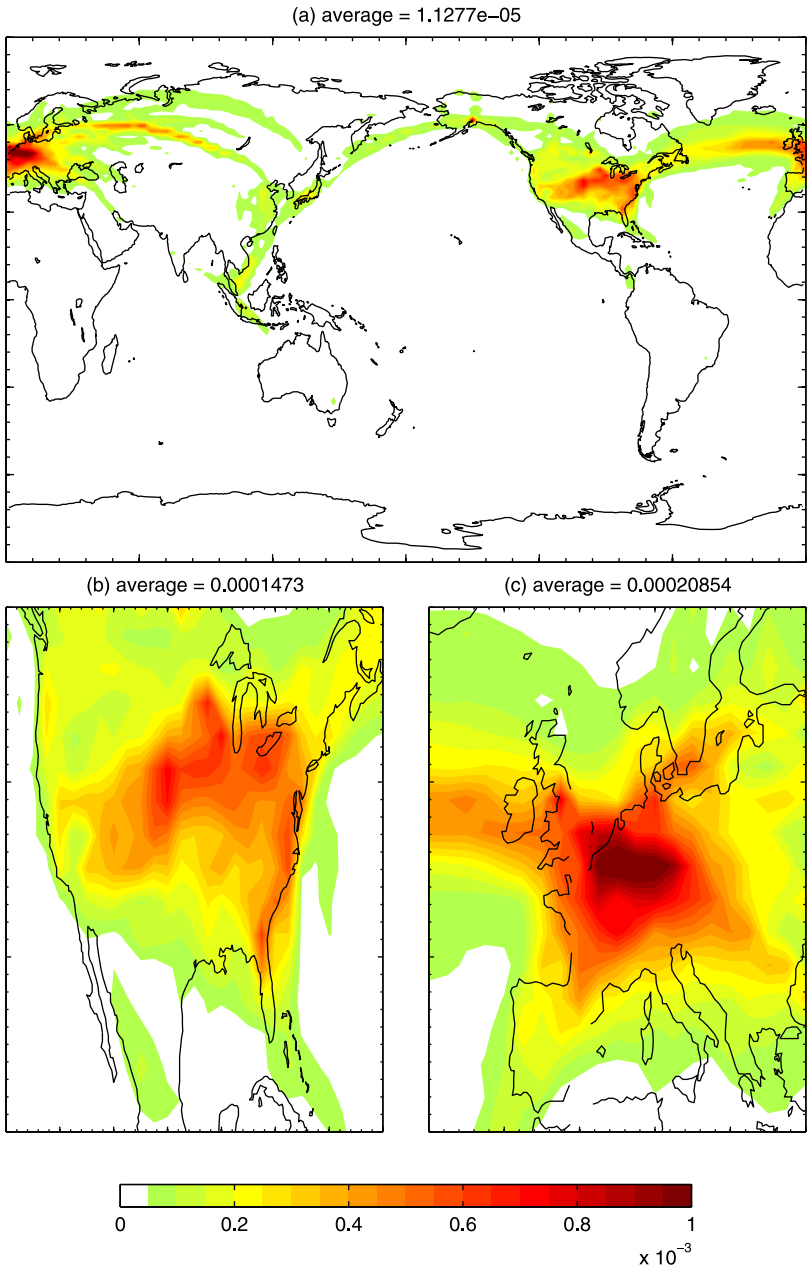

Figure 5. Annually averaged instantaneous increase in cloud fraction due to persistent contrails simulated by CAM5-L82 with an assumption of $\mathcal{C} = 300\ \text{m} \times 300\ \text{m}$. The (a) global and (b, c) regional averages are given at the top of each panel.

[33] The sensitivity of the cross-sectional area ($\mathcal{C}$) on the additional cloud fraction due to contrails can be found in Table 2. It is found that the global average additional cloud fraction nearly doubles when the cross-sectional area is increased from $100\ \text{m} \times 100\ \text{m}$ to $300\ \text{m} \times 300\ \text{m}$.

4.2.3. Sensitivity of Global Contrail Coverage Due to Model Vertical Resolution

[34] The global cloud cover attributed to persistent contrails simulated by CAM5 is sensitive to the vertical resolution of the model. The average additional contrail cloud fraction is increased as vertical resolution increases. This mainly results from the fact that the same amount of additional cloud fraction in one single layer in a lower resolution model is distributed into several shallower layers in a higher resolution model. The maximum random cloud overlap scheme then increases total cloudiness. The global and regional averages of cloud cover associated with persistent contrails are listed in Table 2.

[35] The monthly averaged additional cloud fraction associated with contrails over the globe, continental US, and Western Europe is shown in Figure 7. As noted earlier, cloudiness is enhanced in a higher vertical resolution simulation. The results also reveal less cloudiness during the summer months of the Northern Hemisphere.

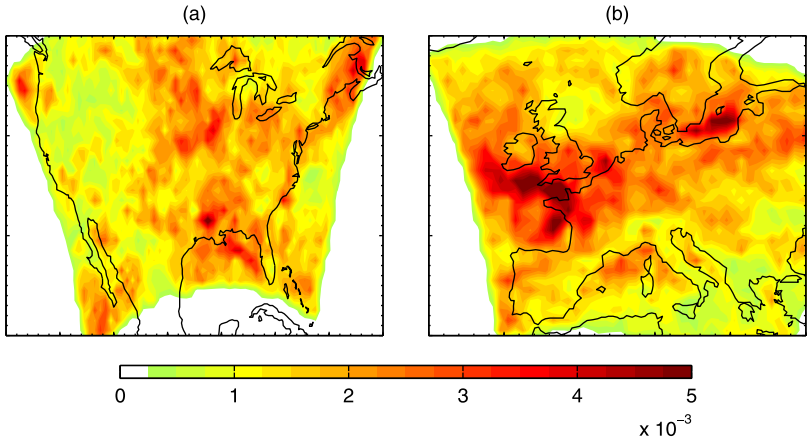

Figure 6. MODIS observations of cloud fraction (in percentage) associated with linear contrails in Jan., Apr., Jul, and Oct. over: (a) continental US, and (b) Europe. (Note: the contour interval is different from Figure 5.)

[36] The resulting evolution of contrails is determined by the model state, and the contrail cloud is treated no differently than any other ice cloud in the model. Ice mass and number will advect. Particles will sediment. If ice supersaturation continues, the contrail cloud will take up ambient humidity and grow. Radiative effects of the cloud are treated the same as other ice cloud optical properties, with the appropriate size distribution. These effects are to be treated and described in subsequent publications.

5. Discussions

[37] In this paper, we have presented how the 2006 ADET dataset is converted from emission mass to mixing ratio tendencies which allows the 2006 ADET emissions to be incorporated in a consistent way to CAM. In particular, we focus on aircraft water vapor emissions and the cloud coverage associated with contrails. To successfully simulate contrails, it is crucial that the numerical model can produce an accurate frequency and distribution of ice supersaturation in the UTLS which CAM5 has demonstrated to achieve.

[38] We have also presented a series of CAM5-SD simulations in which cloudiness associated with contrails is assessed and compared with MODIS retrievals of contrails. It is found that the global amount of contrails simulated by CAM5-SD is sensitive to the vertical resolution in the UTLS. A good agreement in cloud

Table 2. Annually Averaged Cloud Fraction Associated With Contrails in Four Model Configurations (L30, L40, L54 and L82): Global, US and Western European Averages by Assuming the Cross-Sectional Area ($\mathcal{C}$) as 100 m × 100 m and 300 m × 300 m

Vertical Resolution	Global	US	W. Europe
L30	6.0897e-07/1.4154e-06	7.5754e-06/2.1788e-05	1.0723e-05/2.1706e-05
L40	1.7296e-06/3.2570e-06	1.9583e-05/4.5056e-05	3.3357e-05/5.7623e-05
L54	3.3559e-06/5.9218e-06	3.7301e-05/7.9053e-05	6.5387e-05/1.0794e-04
L82	6.6278e-06/1.1277e-05	7.3065e-05/1.4730e-04	1.2953e-04/2.0854e-04

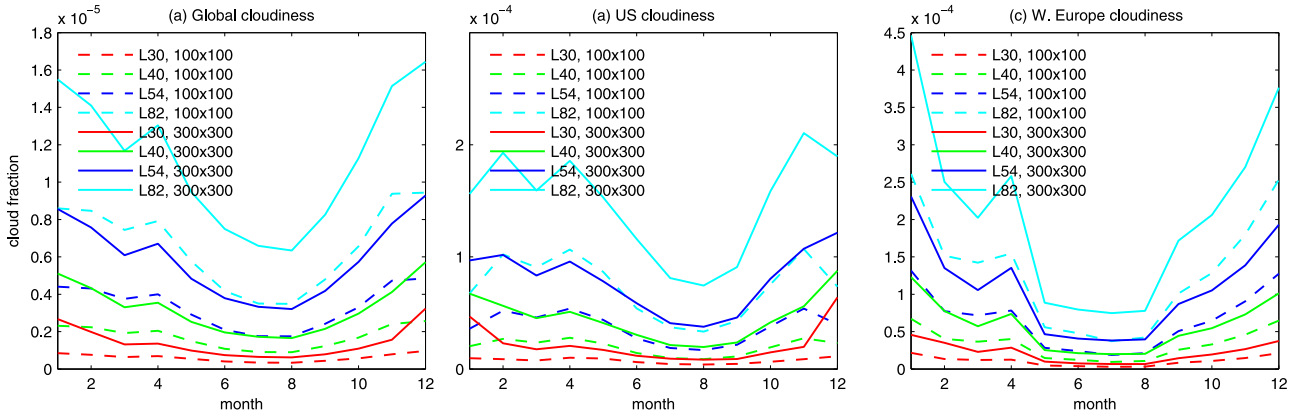

Figure 7. Monthly averaged additional cloud fraction simulated by CAM5 over the: (a) globe, (b) US, and (c) Western Europe, by assuming the cross-sectional area ($\mathcal{C}$) as 100 m × 100 m and 300 m × 300 m.

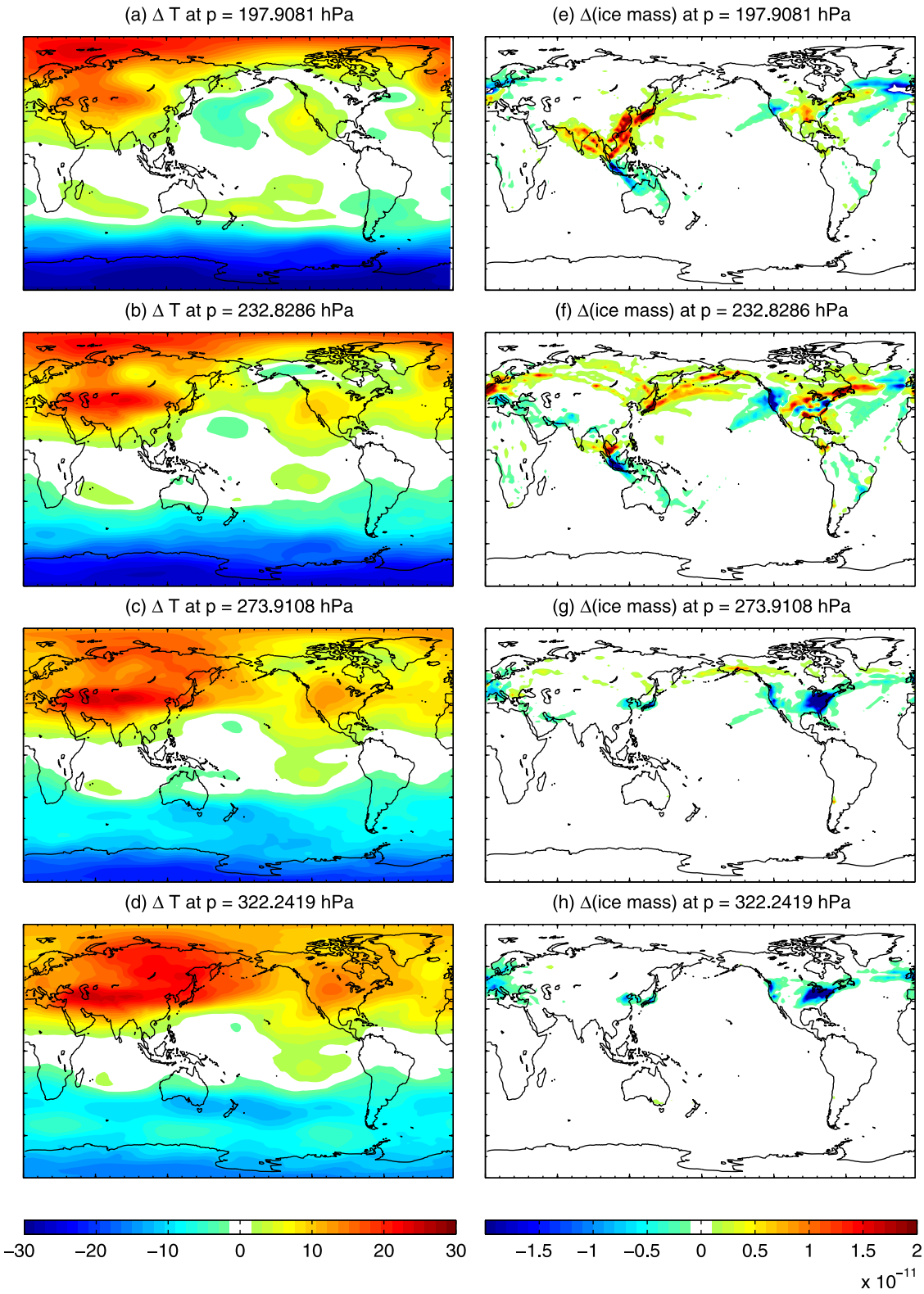

Figure 8. Difference in (a–d) temperature and (e–h) ice mixing ratio of contrails assuming $\mathcal{C} = 100\ \mathrm{m} \times 100\ \mathrm{m}$ between Jul. and Jan. simulated by CAM-SD L30.

cover associated with contrails over the continental US between CAM5-SD simulations and MODIS retrievals may be reached if the vertical layer of CAM5 in the UTLS is less than 5 hPa.

[39] It is found that the global amount of contrails simulated by CESM exhibits a seasonal cycle with maximum/minimum during the winter/summer of the Northern Hemisphere (Figure 7). Higher tropopause altitudes in summer may favor formation of contrails since most aircraft emissions will be injected into the troposphere instead of the stratosphere. Nevertheless, the temperature in the UTLS in summer is significantly higher which makes it much less likely for the ambient temperature to fall below the critical temperature (T_c) and thus the Schmidt-Appleman criterion are not met.

[40] The difference in temperature and ice mixing ratio of contrails simulated by CAM-SD L30 between Jul. and Jan. is illustrated in Figure 8. It is found that the temperature field is significantly warmer in July over the UTLS (Figures 8a–8d). While the higher tropopause in July may enhance the formation of contrails due to higher ambient humidity, as evident at p = 198 hPa (Figure 8e) and 233 hPa (Figure 8f) over the US, even more reduction of contrails is caused by warmer temperature, as seen at p = 274 hPa (Figure 8g) and 322 hPa (Figure 8h). Clearly, the temperature factor dominates the seasonal cycle of contrails and more contrails are found in winter months. This feature is consistent with MODIS observations.

[41] The findings of this study will allow us to proceed with the assessment of the impact of contrails on the climate system, e.g., contrail radiative forcing. In addition to water vapor emissions, aviation impact on climate by other chemical species can also be assessed by using CAM5.

6. Summary

[42] Here we summarize the key findings of the paper:

[43] 1. The model hydrologic cycle of CAM5 is similar to observations for ice supersaturation in the UTLS when compared to AIRS satellite estimates, especially considering the known dry bias of AIRS. Relative humidity and the frequency of supersaturation are reproduced.

[44] 2. The ADET emissions can be added in a consistent way to the hydrologic cycle of CAM. A similar methodology can be used for other aircraft emission species represented in the AEDT emissions database.

[45] 3. CAM5 coupled with our contrail parameterization produces reasonable instantaneous contrail fraction patterns compared to satellite based estimates of linear contrails. The contrail frequency is several times smaller since we do not account for spreading of the contrails over the model time step.

[46] 4. The global ice mass of contrails simulated by CAM5 is stable with respect to the vertical resolution of the model, but the contrail cloud fraction is sensitive to the vertical resolution due to cloud overlap assumptions. Radiative forcing for ice clouds is strongly sensitive to mass in the column (large fraction with low in-cloud ice content produces a similar radiative forcing to small fraction with large ice content). This means that the model should be more stable for estimating radiative forcing despite the sensitivity of ice cloud fraction to vertical resolution.

[47] 5. More contrails are seen in winter than summer due to the warmer atmospheric temperature in summer at flight levels. This reduces the potential for contrail formation.

[48] 6. Future work will use this modeling framework to assess the radiative and chemical forcing of the atmosphere by aircraft emissions.

Appendix

A. How to Incorporate Aircraft Emissions Into CESM

[49] Aircraft emissions can be included in CAM5 from version CESM1.0.2 forward by specifying emission files for different species. A list of input data files and field names to map them onto needs to be supplied in the CAM5 namelist as noted below. All aircraft emissions and distances traveled are handled by the namelist variable *aircraft_specifier* and the data will be stored in *pbuf*. The following example in namelist variables will incorporate emissions of water vapor and carbon dioxide in the CAM5 simulation:

```
aircraft_specifier = 'ac_H2O->/directory/filelist_H2O.dat'
                     'ac_FUELBURN->/directory/
                     filelist_FUELBURN.dat'
```

[50] The "filelist" files are simple text files which list all netCDF files, with full path, of aircraft emission mixing ratio tendencies for the specified species. During the simulation, CESM will search for all listed netCDF files to determine if emission mixing ratio tendencies are available at a given time step. If so, the data will be read into the model and the variables storing the mixing ratio tendencies, in *pbuf* named as "ac_H2O" and "ac_FUELBURN" in the aforementioned example, will be updated.

[51] In this paper, we have presented how we processed the AEDT dataset and the converted monthly averaged aircraft emissions are included in the CESM input data repository. (For more information, please visit http://www.cesm.ucar.edu.) These emissions can be incorporated in CESM1.0.2 and later versions and the source code can be accessed at http://www.cesm.ucar.edu/models/cesm1.0.2/.

[52] **Acknowledgments.** This work was funded by the FAA's ACCRI Program under award DTRT57-10-C-10012. Computing resources were provided by the Climate Simulation Laboratory at National Center for Atmospheric Research (NCAR) Computational and Information Systems Laboratory. NCAR is sponsored by the U.S. National Foundation.

References

Appleman, H. (1953), The formation of exhaust condensation trails by jet aircraft, *Bull. Am. Meteorol. Soc.*, *34*, 14–20.

Burkhardt, U., B. Kärcher, M. Ponater, K. Gierens, and A. Gettelman (2008), Contrail cirrus supporting areas in model and observations, *Geophys. Res. Lett.*, *35*, L16808, doi: 10.1029/2008GL034056.

Burkhardt, U., B. Kärcher, and U. Schumann (2010), Global modeling of the contrail and contrail cirrus climate impact, *Bull. Am. Meteorol. Soc.*, *91*, 479–483, doi: 10.1175/2009BAMS2656.1.

Carpenter, R. L., JrK. K. Droegemeier, P. R. Woodward, and C. E. Hane (1990), Application of the piecewise parabolic method (PPM) to meteorological modeling, *Mon. Weather Rev.*, *118*, 586–612, doi: 10.1175/1520-0493(1990)118<0586:AOTPPM>2.0.CO;2.

Colella, P., and P. R. Woodward (1984), The piecewise parabolic method (PPM) for gas-dynamical simualtions, *J. Comput. Phys.*, *54*, 174–201, doi: 10.1016/0021-9991(84)90143-8.

Duda, D. P., R. Palikonda, T. Chee, and P. Minnis (2011), A MODIS-based contrail climatology of coverage and cloud properties, paper presented at the 15th Conference on Aviation, Range, and Aerospace Meteorology, Am. Meteorol. Soc., Los Angeles, Calif., 1–4 Aug.

Easter, R. C., S. J. Ghan, Y. Zhang, R. D. Saylor, E. G. Chapman, N. S. Laulainen, H. Abdul-Razzak, L. R. Leung, X. Bian, and R. A. Zaveri (2004), MIRAGE: Model description and evaluation of aerosols and trace gases, *J. Geophys. Res.*, *109*, D20210, doi: 10.1029/2004JD004571.

Gettelman, A., and S. L. Baughcum (1999), Direct deposition of subsonic aircraft emissions into the stratosphere, *J. Geophys. Res.*, *104*, 8317–8327, doi: 10.1029/1999JD900070.

Gettelman, A., E. J. Fetzer, F. W. Irion, and A. Eldering (2006), The global distribution of supersaturation in the upper troposphere, *J. Clim.*, *19*, 6089–6103, doi: 10.1175/JCLI3955.1.

Gettelman, A., H. Morrison, and S. J. Ghan (2008), A new two-moment bulk stratiform cloud microphysics scheme in the Community Atmospheric Model (CAM3), Part II: single-column and global results, *J. Clim.*, *21*, 3660–3679, doi: 10.1175/2008JCLI2116.1.

Gettelman, A., X. Liu, S. J. Ghan, H. Morrison, S. Park, A. J. Conley, S. A. Klein, J. Boyle, D. L. Mitchell, and J.-LF. Li (2010), Global simulations of ice nucleation and ice supersaturation with an improved cloud scheme in the Community Atmosphere Model, *J. Geophys. Res.*, *115*, D18216, doi: 10.1029/2009JD013797.

Hartmann, D. L., M. E. Ockert-Bell, and M. L. Michelsen (1992), The effect of cloud type on Earth's energy balance: Global analysis, *J. Clim.*, *5*, 1281–1304, doi: 10.1175/1520-0442(1992)005<1281:TEOCTO>2.0.CO;2.

Henderson, S. C., et al. (1999), Aircraft emissions: Current inventories and future scenariosin, in *Aviation and the Global Atmosphere. Special Report of the Intergovernmental Panel on Climate Change*, edited by J. E. Penner et al., chap. 9, pp. 290–331, Cambridge Univ. Press, Cambridge, U. K.

Iacono, M. J., J. S. Delamere, E. J. Mlawer, M. W. Shephard, S. A. Clough, and W. D. Collins (2008), Radiative forcing by long-lived greenhouse gases: Calculations with the AER radiative transfer models, *J. Geophys. Res.*, *113*, D13103, doi: 10.1029/2008JD009944.

Kärcher, B., O. M. amd P. J. DeMott, S. Pechtl, and F. Yu (2007), Insights into the role of soot aerosols in cirrus cloud formation, *Atmos. Chem. Phys.*, *7*, 4203–4227, doi: 10.5194/acp-7-4203-2007.

Kim, B. Y., et al. (2007), System for assessing Aviation's Global Emissions (SAGE), part I: Model description and inventory results, *Transp. Res., Part D*, *12*, 325–346, doi: 10.1016/j.trd.2007.03.007.

Lee, D. S., et al. (2010), Transport impacts on atmosphere and climate: Aviation, *Atmos. Environ.*, *44*, 4678–4734, doi: 10.1016/j.atmosenv.2009.06.005.

Lee, J. J., I. A. Waitz, B. Y. Kim, G. G. Fleming, L. Q. Maurice, and C. A. Holsclaw (2007), System for assessing Aviation's Global Emissions (SAGE), part II: Uncertainty assessment, *Transp. Res., Part D*, *12*, 381–395, doi: 10.1016/j.trd.2007.03.006.

Liu, X., et al. (2011), Toward a minimal representation of aerosol direct and indirect effects: Model description and evaluation, *Geosci. Model Dev. Discuss.*, *4*, 3485–3598, doi: 10.5194/gmdd-4-3485-2011.

Mannstein, H., R. Meyer, and P. Wendling (1999), Operational detection of contrails from NOAA-AVHRR data, *Int. J. Remote Sens.*, *20*, 1641–1660, doi: 10.1080/014311699212650.

Marquart, S., and B. Mayer (2002), Towards a reliable GCM estimation of contrail radiative forcing, *Geophys. Res. Lett.*, *29*(8), 1179, doi: 10.1029/2001GL014075.

Meerkötter, R., U. Schumann, D. R. Doelling, P. Minnis, T. Nakajima, and Y. Tsushima (1999), Radiative forcing by contrails, *Ann. Geophys.*, *17*, 1080–1194, doi: 10.1007/s00585-999-1080-7.

Meyer, R., H. Mannstein, R. Meerkötter, U. Schumann, and P. Wendling (2002), Regional radiative forcing by line-shaped contrails derived from satellite data, *J. Geophys. Res.*, *107*(D10), 4104., doi: 10.1029/2001JD000426.

Minnis, P., D. F. Young, D. P. Garber, L. Nguyen, W. L. Smith Jrand R. Palikonda (1998), Transformation of contrails into cirrus during SUCCESS, *Geophys. Res. Lett.*, *25*, 1157–1160, doi: 10.1029/97GL03314.

Minnis, P., U. Schumann, D. R. Doelling, K. M. Gierens, and D. W. Fahey (1999), Global distribution of contrail radiative forcing, *Geophys. Res. Lett.*, *26*, 1853–1856, doi: 10.1029/1999GL900358.

Minnis, P., R. Palikonda, B. J. Walter, J. K. Ayers, and H. Mannstein (2005), Contrail properties over the eastern North Pacific from AVHRR data, *Meteorol. Z.*, *14*, 515–523, doi: 10.1127/0941-2948/2005/0056.

Minnis, P., D. Duda, R. Palikonda, S. T. Bedka, R. Boeke, K. Khlopenkov, T. Chee, and K. T. Bedka (2011), Estimating contrail climate effects from satellite data, paper presented at the 3rd AIAA Atmospheric Space Environments Conference, Am. Inst. of Aeronaut. and Astronaut., Honolulu, Hawaii, 27–30 June.

Morrison, H., and A. Gettelman (2008), A new two-moment bulk stratiform cloud microphysics scheme in the Community Atmospheric Model (CAM3), part I: Description and numerical tests, *J. Clim.*, *21*, 3642–3659, doi: 10.1175/2008JCLI2105.1.

Myhre, G., and F. Stordal (2001), On the tradeoff of the solar and thermal infrared radiative impact of contrails, *Geophys. Res. Lett.*, *28*, 3119–3122, doi: 10.1029/2001GL013193.

Naiman, A. D., S. K. Lele, and M. Z. Jacobson (2011), Large eddy simulations of contrail development: Sensitivity to initial and ambient conditions over first twenty minutes, *J. Geophys. Res.*, *116*, D21208, doi: 10.1029/2011JD015806.

Neale, R. B., et al. (2010), Desciption of the NCAR Community Atmosphere Model (CAM 5.0), NCAR Tech. Note NCAR/TN-486+STR, Natl. Cent. for Atmos. Res., Boulder, Colo. [Available at http://www.cesm.ucar.edu/models/cesm1.0/cam/docs/description/cam5_desc.pdf.]

Palikonda, R., P. Minnis, D. P. Duda, and H. Mannstein (2005), Contrail coverage derived from 2001 AVHRR data over the continental United States of America and surrounding area, *Meteorol. Z.*, *14*, 525–536, doi: 10.1127/0941-2948/2005/0051.

Penner, J. E., D. H. Lister, D. J. Griggs, D. J. Dokken, and M. McFarland (1999), *Aviation and the Global Atmosphere*, Cambridge Univ. Press, Cambridge, U. K.

Ponater, M., S. Marquart, and R. Sausen (2002), Contrails in a comprehensive global climate model: Parameterization and radiative forcing results, *J. Geophys. Res.*, *107*(D13), 4164., doi: 10.1029/2001JD000429.

Rädel, G., and K. P. Shine (2008), Radiative forcing by persistent contrails and its dependence on cruise altitudes, *J. Geophys. Res.*, *113*, D07105, doi: 10.1029/2007JD009117.

Schmidt, E. (1941), Die Entstehung von Eisnebel aus den Auspuffgasen von Flugmotoren, *Schr. Dtsch. Akad. Luftfahrtforsch.*, *44*, 1–15.

Schröder, F., B. Kärcher, C. Duroure, J. Strom, A. Petzold, J.-F. Gayet, and B. Strauss (2000), On the transition of contrails into cirrus clouds, *J. Atmos. Sci.*, *57*, 464–480, doi: 10.1175/1520-0469(2000)057<0464:OTTOCI>2.0.CO;2.

Schumann, U. (1996), On conditions for contrail formation from aircraft exhausts, *Meteorol. Z.*, *5*, 4–24.

Schumann, U. (2002), Contrail cirrus, in *Cirrus*, edited by D. K. Lynch et al., pp. 231–255, Oxford Univ. Press, Oxford. U. K.

Stephens, G. L., and P. J. Webster (1981), Clouds and climate: Sensitivity of simple systems, *J. Atmos. Sci.*, *38*, 235–247, doi: 10.1175/1520-0469(1981)038<0235:CACSOS>2.0.CO;2.

Wilkerson, J. T., M. Z. Jacobson, A. Malwitz, S. Balasubramanian, R. Wayson, G. Fleming, A. D. Naiman, and S. K. Lele (2010), Analysis of emission data from global commercial aviation: 2004 and 2006, *Atmos. Chem. Phys. Discuss.*, *10*, 2945–2983, doi: 10.5194/acpd-10-2945-2010.

C.-C. Chen, C. Craig, and A. Gettelman, National Center for Atmospheric Research, PO Box 3000, Boulder, CO 80307-3000, USA. (cchen@ucar.edu)

D. P. Duda, Science Systems and Applications, Inc., 1 Enterprise Pkwy., Ste. 200, Hampton, VA 23666, USA.

P. Minnis, NASA Langley Research Center, 21 Langley Blvd., Hampton, VA 23681, USA.